Multiscale Sensing of Antibody–Antigen Interactions by Organic Transistors and Single-Molecule Force Spectroscopy

Stefano Casalini,[*,†] Andra C. Dumitru,[‡] Francesca Leonardi,[§,∥] Carlo A. Bortolotti,[†] Elena T. Herruzo,[‡] Alessandra Campana,[§,⊥] Rafael F. de Oliveira,[†,#] Tobias Cramer,[§,∞] Ricardo Garcia,[*,‡] and Fabio Biscarini[†,§]

[†]Dipartimento di Scienze della Vita, Università degli Studi di Modena e Reggio Emilia, Via Campi 183, 41125 Modena, Italy, [‡]Instituto de Ciencia de Materiales de Madrid (CSIC), 28049 Madrid, Spain, [§]Istituto per lo Studio dei Materiali Nanostrutturati (ISMN) and [∥]Istituto per la Sintesi Organica e Fotoreattività (ISOF), Consiglio Nazionale delle Ricerche (CNR), Via Gobetti 101, 40129 Bologna, Italy, [⊥]"Alma Mater Studiorum", Dipartimento di Chimica "G. Ciamician", Università di Bologna, Via Selmi 2, 40126 Bologna, Italy, [#]Unesp, Postgraduate Program in Materials Science and Technology, São Paulo State University, 17033-360, Bauru, SP Brazil, and [∞]"Alma Mater Studiorum", Dipartimento di Fisica e Astronomia, Università di Bologna, Viale Berti Pichat 6/2, 40127 Bologna, Italy

ABSTRACT Antibody–antigen (Ab–Ag) recognition is the primary event at the basis of many biosensing platforms. In label-free biosensors, these events occurring at solid–liquid interfaces are complex and often difficult to control technologically across the smallest length scales down to the molecular scale. Here a molecular-scale technique, such as single-molecule force spectroscopy, is performed across areas of a real electrode functionalized for the immunodetection of an inflammatory cytokine, *viz.* interleukin-4 (IL4). The statistical analysis of force–distance curves allows us to quantify the probability, the characteristic length scales, the adhesion energy, and the time scales of specific recognition. These results enable us to rationalize the response of an electrolyte-gated organic field-effect transistor (EGOFET) operated as an IL4 immunosensor. Two different strategies for the immobilization of IL4 antibodies on the Au gate electrode have been compared: antibodies are bound to (i) a smooth film of His-tagged protein G (PG)/Au; (ii) a 6-aminohexanethiol (HSC_6NH_2) self-assembled monolayer on Au through glutaraldehyde. The most sensitive EGOFET (concentration minimum detection level down to 5 nM of IL4) is obtained with the first functionalization strategy. This result is correlated to the highest probability (30%) of specific binding events detected by force spectroscopy on Ab/PG/Au electrodes, compared to 10% probability on electrodes with the second functionalization. Specifically, this demonstrates that Ab/PG/Au yields the largest areal density of oriented antibodies available for recognition. More in general, this work shows that specific recognition events in multiscale biosensors can be assessed, quantified, and optimized by means of a nanoscale technique.

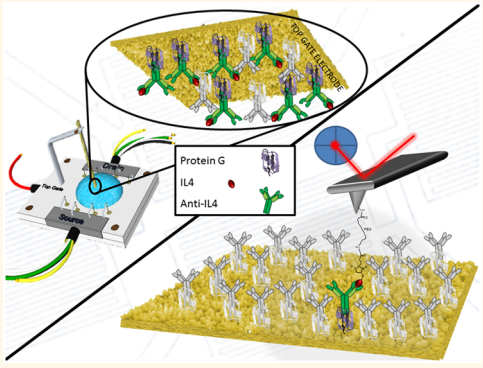

KEYWORDS: organic field-effect transistors · immunosensing · interleukin-4 · single-molecule force spectroscopy · atomic force microscopy · biorecognition · bioelectronics

Immunosensing exploits one of nature's most optimized molecular recognition mechanisms, namely, the interaction between an antigen (Ag) and its specific antibody (Ab).[1] The large binding constant is exploited in enzyme-linked immunosorbent assay (ELISA) to detect the presence of biomarkers in bodily fluids whose concentration can be below picomolar level.[2]

Detecting Ab–Ag interactions with a label-free sensing scheme requires the integration of biorecognition moieties at a solid–liquid interface and their coupling with the transducer. The transduction of the molecular binding event should occur with minimum, if any, further chemical amplification or development steps.[3] This is particularly relevant for point-of-care applications and in-field deployed sensors. Sensitivity and specificity both depend on how the biorecognition groups are made available to the target and on the coupling between environment and transducer.

Among label-free immunosensors, mechanical and electronic transductions have been demonstrated.[4−8] In the case of an electronic sensor, several phenomena induced by the biorecognition event might be exploited: local changes of electrostatic potential,[9] density of charge carriers,

* Address correspondence to stefano.casalini@unimore.it, r.garcia@csic.es.

Received for review January 8, 2015 and accepted April 13, 2015.

Published online April 13, 2015
10.1021/acsnano.5b00136

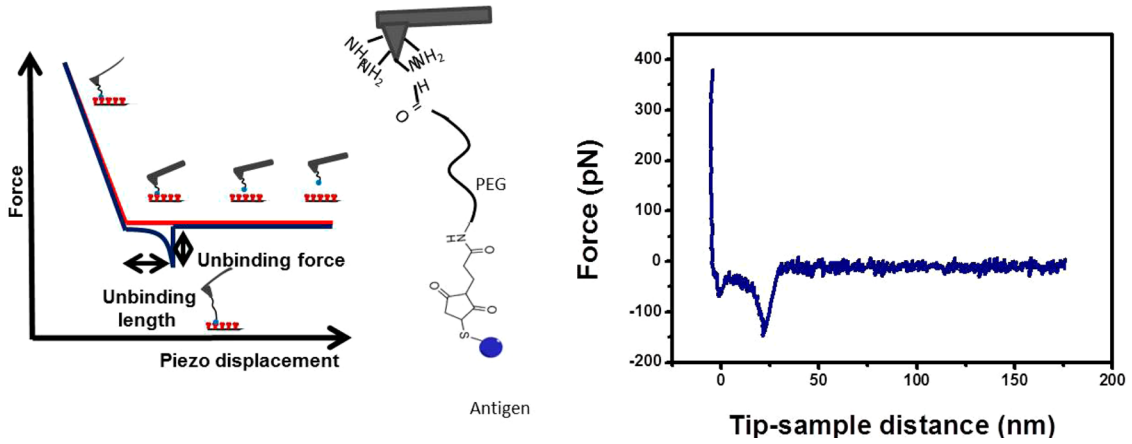

Figure 1. (Left) Schematics of a force–distance plot (force curve). As the tip approaches the sample and the contact is established, the repulsive forces cause the tip to bend upward (red line). The tip is then retracted (blue line). If a recognition event occurs, adhesion forces will make the tip bend downward during retraction. When force gradient exceeds the spring constant of the cantilever, the probe jumps out of contact to its initial position. The unbinding force of the antibody–antigen pair is the maximum adhesive force, estimated as the vertical difference between the baseline and the minimum force at retraction. Unbinding length is the difference between the tip–sample distance where the unbinding event occurs and the contact point. Discrimination of specific and nonspecific binding events relies on the estimate of the gradient of the force near the detachment point. Details are found in Supporting Information. (Center) Scheme of the AFM tip functionalization. IL4–PEG linker complex is attached to an amino-functionalized AFM tip. (Right) Real force curve shows a specific unbinding event.

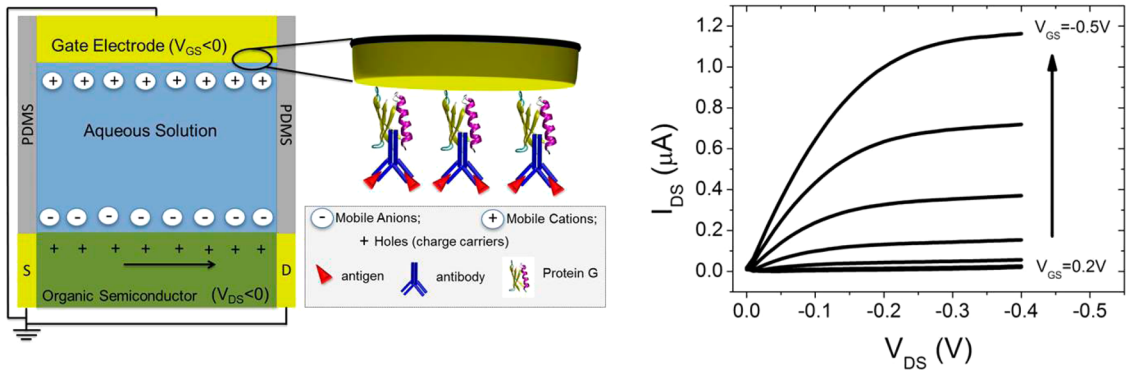

Figure 2. Left: Schematic EGOFET cross section along with a sketch of the magnification of the gate/electrolyte interface. Right: *I*–*V* output characteristics of a reference device.

conductivity,[10] impedance,[11] and capacitance.[12] Simplicity of instruments and low cost are factors that make electronic transduction favored for single-shot applications.[13] Device sensitivity is optimized by tuning the Debye length scale in fluids to the size of the specific binding pair by modulation of ionic strength. However, such modulation is not always doable,[14–16] especially in bodily fluids.

Mechanical sensors, such as quartz crystal microbalance (QCM)[5] and cantilevers,[6] detect changes of mass, binding/unbinding forces, and viscoelastic response. They are effective in those regimes where electronic sensing does not provide enough sensitivity. However, the interpretation of the device output in terms of specific molecular interactions is not usually straightforward.

Quantification, reproducibility, and standardization are open issues in label-free immunosensing. They require multiscale control from nanometer to hundreds of micrometers of the density, orientation, and functionality of the recognition moieties on the sensing area of the device. Open questions that also represent technological challenges include how to control the density of active Abs; what fraction of Abs gives rise to specific biorecognition events; what is the detection limit of the device in terms of number of recognition events; how to make the device more effective, sensitive, and specific.

In this paper, we propose a multiscale approach where local and nonlocal techniques sensitive to antibody–antigen recognition events are combined for quantitatively understanding and developing a label-free biosensor. Our approach combines single-molecule force spectroscopy (SFS) (see Figure 1) and an electrolyte-gated organic field-effect transistor (EGOFET) (see Figure 2) to assess specific recognition on device-relevant Au surfaces in the limit of a strong electrostatic screening regime.

SFS is sensitive to a few single antibody–antigen interactions. In SFS, the force dependence on the

probe−surface distance, termed force curve, is recorded. A force curve exhibits regions where a smooth variation *versus* the distance is interrupted by abrupt changes. These "jumps" are interpreted as the rupture of single or multiple bonds that were formed because of molecular recognition interactions. The value of the forces measured by SFS depends on both the loading rate[17,18] and the relevant electrostatic interactions.[19] With the latter being anisotropic, the orientation of the recognition moiety on the surface is important. This orientation may substantially vary depending on the protocol adopted for immobilizing the recognition group on the surface. SFS has been successfully applied to measure the forces between ligands and receptors,[20,21] antibody−antigen,[22,23] to investigate the unfolding of proteins,[24] protein stability,[25] the interaction between carbohydrates,[26] and cell adhesion.[27] As a result, SFS has been crucial to systematically check the effective immunorecognition due to different adhesion layers.

These surface treatments have been used to functionalize the EGOFET gate electrode that, when immersed in the electrolyte solution, binds and detects the biomolecule of interest. A number of local binding events occurs at the gate electrode, leading to a potential change.[28−30] This change affects the electrostatic potential at the electrolyte solution/organic semiconductor interface, which couples to the semiconductor channel *via* the capacitance C_{DL} of the Debye−Helmholtz layer. With C_{DL} on the order of 10−20 μF/cm^2,[31] EGOFET responds to changes of potential as low as 50−100 μV.[32] These correspond approximately to a few recognition events per 100 × 100 nm^2 area of the device. Considering an active channel area $A = W \times L$ given by width W multiplied by length L, EGOFET with $A = 0.5$ mm^2 responds to 10−100 million recognition events occurring on the device. EGOFETs were shown to transduce signals in neuronal cell populations, sub-nanomolar concentration of neurotransmitters[33] and DNA,[34] local pH changes (9 mV/pH),[35] penicillin,[36] and biotin−streptavidin hybridization.[37] In this work, we use an EGOFET with a 15 nm thick pentacene film as the transport channel.

Here, the analytical target is interleukin-4 (IL4), an anti-inflammatory cytokine relevant in several pathologies.[38−41] The specific recognition moiety is IL4 monoclonal antibody that is immobilized on the gate electrode by means of two distinct strategies. The first is based on a 6-aminohexanethiol (HSC_6NH_2) monolayer activated by glutaraldehyde.[42,43] This functional approach guarantees chemical binding between Au and the side chains of the lysine residues in the Ab; however, there is no control on the Ab orientation due to the natural abundance of lysine in the Ab backbone. The second strategy exploits the recombinant His-tagged PG, whose N-terminus side is tailored by a 6-histidine chain (6-His-tag). His-tags are well-known to be bound on polycrystalline Au.[44,45] This affinity was already exploited for the fabrication of nanomechanical motors based on the grafting of F1-ATPase on gold substrates.[46] His-tagged PG forms an oriented layer which promotes Ab immobilization on the Au electrode.[47] Neutron reflectometry, light interferometry, and ellipsometry show that Abs on PG-functionalized ideal surfaces form smooth monolayers.[48] Antibodies are oriented by the specific interaction of PG with the fragment crystallizable region (Fc) that forces Ab to expose its binding sites to the environment.[49,50]

Both SFS and EGOFET show substantial differences of sensitivity between the two immobilization strategies. SFS experiments yield a larger probability of specific recognition events ($P_{sb} \approx 30\%$) occurring on PG-functionalized electrodes with respect to the control samples ($P_{sb} < 10\%$). The PG-functionalized EGOFET detects changes of charge mobility and threshold voltage for IL4 concentrations as low as 5 nM. No change is detected for HSC_6NH_2-functionalized EGOFET.

These results show the direct correlation between SFS measurements at the single-molecule level and the electronic response of the EGOFET that is caused by a change of electrostatic potential on the square millimeter channel. This approach can lead to a methodology for designing, developing, and optimizing label-free biosensors.

RESULTS AND DISCUSSION

Electrochemical Measurements. The result of Au functionalization was first assessed by cyclic voltammetry and impedance spectroscopy (see Figure 3) by monitoring the changes in the faradaic response of the ferricyanide redox probe, $[Fe(CN)_6]^{3-/4-}$. In the case of HSC_6NH_2-functionalized Au electrodes, cyclic voltammetry displays an increase of the peak-to-peak distance from 60 to >250 mV upon changing the pH of the solution from neutral to basic values (Figure 3a). This indicates a dramatic slowing down of the electron transfer not observed on bare Au that is consistent with the presence of the amino-terminated SAM (self-assembled monolayer) on the electrode surface.[51]

We monitored PG adsorption onto polycrystalline Au electrodes by means of impedance spectroscopy (Figure 3b). The data fitted with Randles circuit (see Experimental Methods) show that the capacitance (C_{DL}) decreases from 11.3 ± 0.2 to 2.1 ± 0.1 μF, and the charge transfer resistance (R_{CT}) increases from 12.8 ± 0.2 to 270 ± 3 Ω. This indicates that PG is adsorbed onto the Au electrode. The orientation of the adsorbed PG is assessed by measuring the impedance changes upon incubation of the PG-functionalized electrode in a 400 mM imidazole solution for 30 min. We observe a capacitance increase to 2.7 ± 0.1 μF, along with a dramatic decrease of R_{CT} down to 63 ± 0.1 Ω (see Supporting Information Figure S1). These changes show partial desorption of His-tagged PG

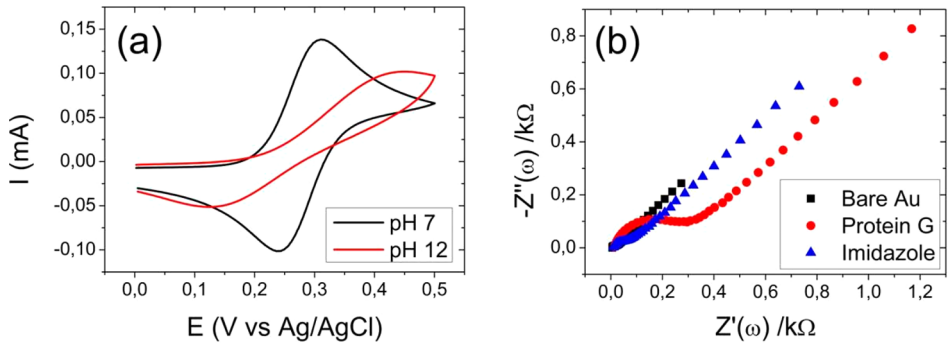

Figure 3. (a) Cyclic voltammograms of the ferricyanide signal at neutral and basic pH at a polycrystalline gold electrode functionalized with HSC_6NH_2. (b) Impedance spectroscopy for bare Au (black filled squares), PG adsorption (red filled circles), and PG elution mediated by imidazole exposure (blue filled triangles).

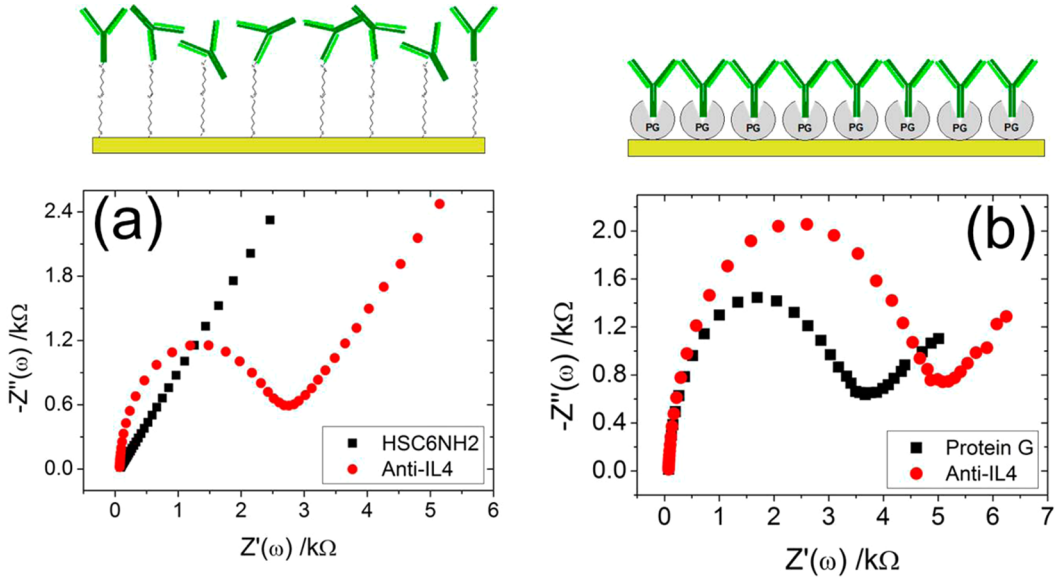

Figure 4. Nyquist plots of (a) HSC_6NH_2- and (b) PG-mediated treatment. On the top part of these plots, a cartoon of the two functionalization strategies is shown.

from the gold electrode, thus proving that the His-tag mediates the PG assembly on Au (see Figure 3b).

Both strategies are effective for immobilizing anti-IL4 on the surface, as apparent from Figure 4 and the data reported in Table S1. For both electrode functionalizations, we observe a significant increase of the charge transfer resistance R_{CT} upon incubation in anti-IL4 solution. The capacitance change is consistent with the Ab adsorption for the HSC_6NH_2-functionalized electrode. The capacitance exhibits no significant change in the case of the PG-functionalized electrode.

Tapping Mode AFM. The ability of both functionalization protocols to lead to Ab immobilization onto the gold substrate has been evaluated by tapping mode AFM in air and phosphate buffer solution (PBS). The surface topography of a typical bare gold sample recorded in air is displayed in Figure 5a. The sample consists of a few tens of nanometers in diameter gold grains formed by thermal sublimation, with a maximum height of 10 nm and root-mean-square (rms) roughness of 1.1 nm. PG adsorption (Figure 5b) yields a smoother surface of reduced height and roughness. Incubation of the sample with the anti-IL4 solution leads to an increase of the maximum height by 3.5 nm and roughness by 0.39 nm (Figure 5c). The height difference is in good agreement with the size of IgG antibodies adsorbed with an orientation consistent with the so-called Y configuration in air as previously reported.[52]

The rms roughness for the different functionalization steps (Figure 5d) follows the same trend both in air and in PBS. There is a decrease upon PG deposition that is followed by an increase of 0.39 nm in air and 0.61 nm in PBS as a result of the antibody immobilization.

Single-Force Spectroscopy. After the successful immobilization of anti-IL4 on modified gold substrates was assessed, biomolecular recognition was studied by means of SFS using probes functionalized with IL4 linked to the tip by a flexible PEGylated chain (see Experimental Methods). The binding forces between the specific probe and anti-IL4 bound to the electrode surface were extracted from a series of repeated force

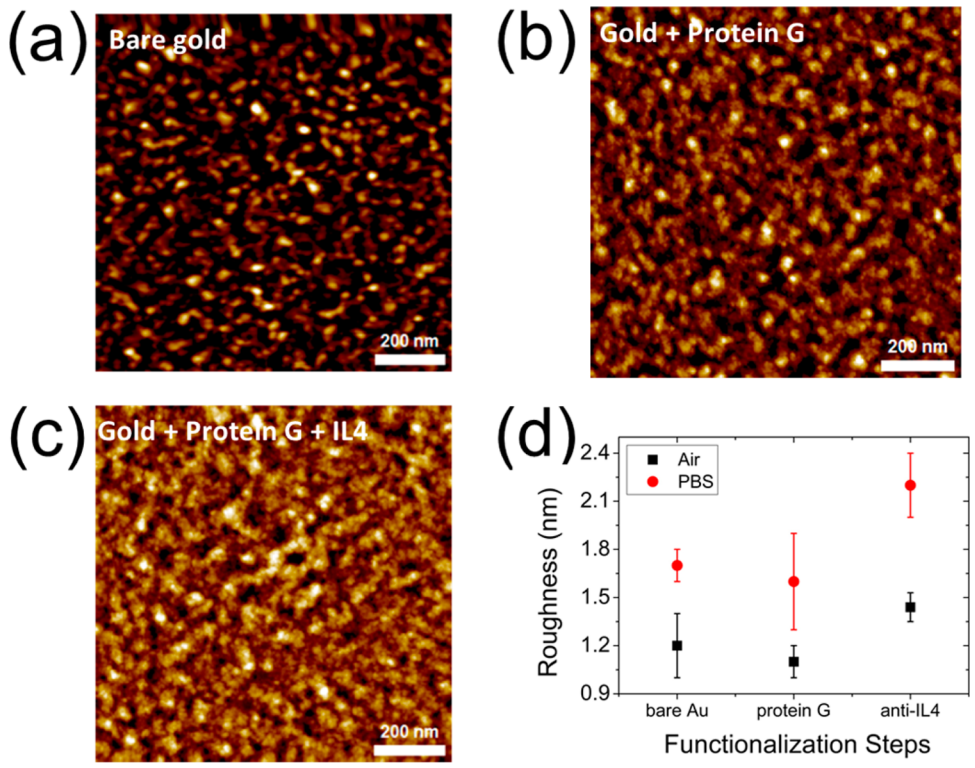

Figure 5. AFM images on bare gold (a), PG-coated gold (b), PG/anti-IL4-coated gold (c). Roughness data are overlaid in air and in PBS solution (d).

curves acquired on a 32 × 32 points grid on an area of 1 μm × 1 μm (see Experimental Methods).

Figure 6a,b shows the 2D histograms containing the number of events with a given unbinding force (F_{ub}) and unbinding length (L_{ub}) for PG- and HSC_6NH_2-functionalized electrodes, respectively. These histograms cluster together the curves with similar values for the unbinding forces and unbinding distance. Each point (represented as a hexagon) in the 2D histograms contains the force curves corresponding to different types of events. As an example, Figure 6c,d shows a representative force curve for one of the hexagons in Figure 6a,b. The noisy and adhesive behavior observed in the force curves is related to the fact that the measurements were performed on a real technological surface like polycrystalline gold, instead of prototypical substrates such as mica, which is atomically flat on large areas and more homogeneous.

Regarding unbinding lengths, all events occur in the 20−40 nm range with a dispersion ranging from 10 to >50 nm, corresponding to the PG-coated Au surface. The most probable unbinding lengths occur in the 10−20 nm range with dispersion ranging from 10 to 35 nm for the anti-IL4/HSC_6NH_2/Au surface. We infer that for PG/Au electrodes unbinding events are more spread out at different lengths, and their unbinding distance is further away from the surface. This observation is consistent with the presence of a larger fraction of oriented antibodies in a standing Y-shape configuration[53] since, in this case, we expect that the unbinding event takes place further away from the surface. Additionally, the Fab fragments of an IgG antibody are linked to the Fc fragment through disulfide bonds, resulting in an increased flexibility of these fragments.[54] Thus, an antibody in Y-shape configuration is less constrained by the substrate, which explains the broader distribution of unbinding events as a function of distance in the case of highly oriented anti-IL4. For HSC_6NH_2 functionalization, our results suggest that the anti-IL4 is randomly oriented.

We then performed a statistical analysis of the large data set of unbinding forces, F_{ub}. As shown in Figure 6e, both anti-IL4/PG/Au and anti-IL4/HSC_6NH_2/Au, along with the cross-check sample (namely, tip functionalized with IL6 and Au electrode coated with anti-IL4), yield apparently skewed histograms of F_{ub}. This is not surprising because the data sets have been filtered out of the aspecific events occurring at $F_{ub} \leq 20$ pN. The size of the bin of each histogram is calculated depending on the number of curves, N_{SB}, in the data set, giving rise to (high-force) specific (un)binding (SB). This number changes from sample to sample, and therefore, the sizes of histograms in Figure 6 are different. Specifically, the number of bins in each histogram is chosen as $N_{bin} = \mathrm{NINT}(3.49 \cdot \sigma / N_{SB}^{1/3})$, with NINT being the nearest integer round-off and σ the standard deviation of the data set. The bin size of each histogram is given by $\Delta F = (F_{max} - F_{min})/N_{bin}$, where F_{max} and F_{min} are the boundary values of the force range measured experimentally. The value of the histogram is normalized to

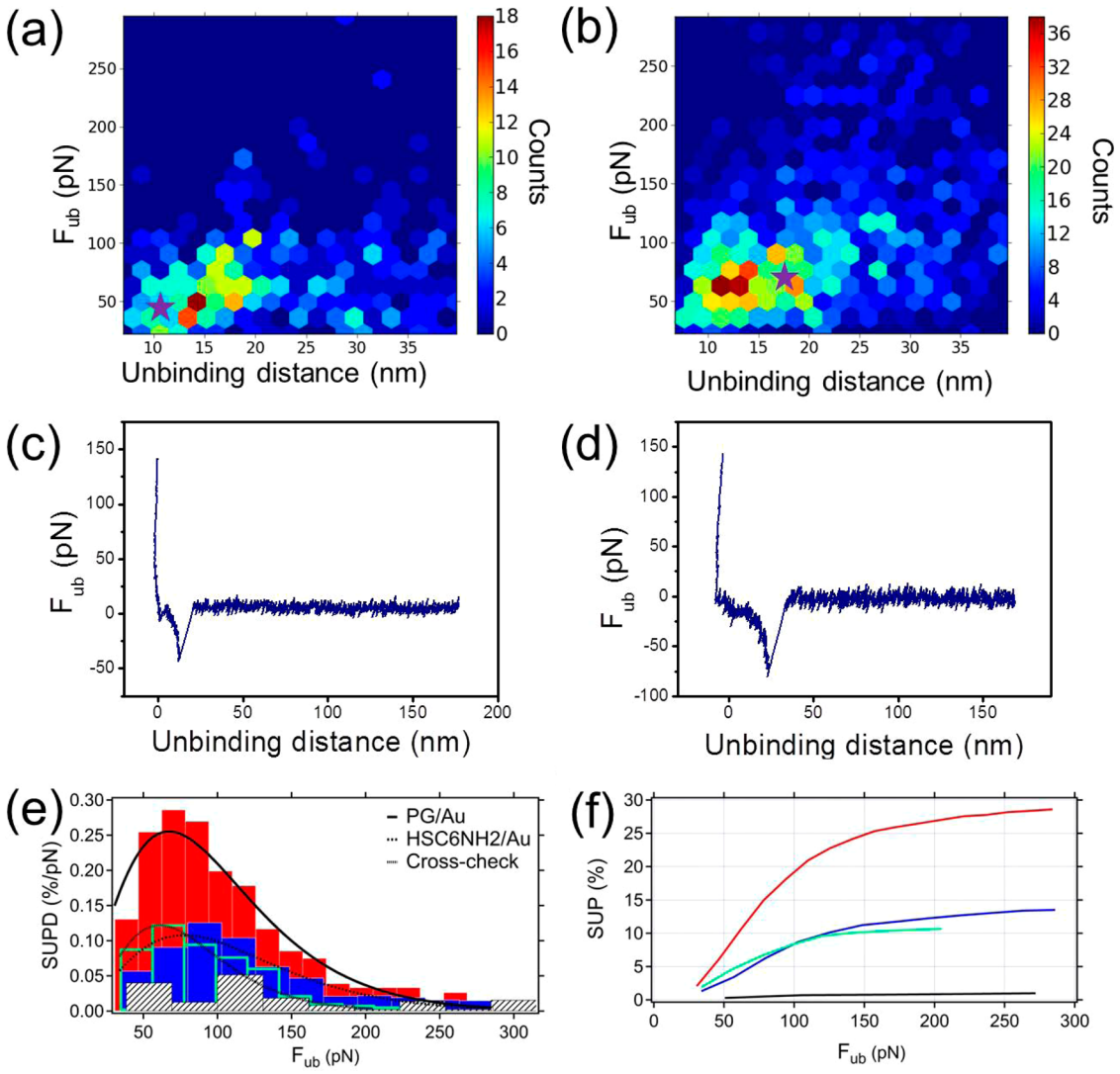

Figure 6. Two-dimensional histograms of the unbinding distance and unbinding force for (a) HSC_6NH_2-based protocol and (b) PG-based one. (c,d) Two representative force *vs* distance curves corresponding to the starred hexagons in (a) and (b). (e) Histograms of SUPD as a function of F. Red, blue, empty, and white-black patterned bars are for PG, HSC_6NH_2, cross-check, and bare Au, respectively. Solid, dashed, and dotted lines are the best χ^2 fits corresponding to PG, HSC_6NH_2, and cross-check. (f) SUP *vs* F plots are shown for each protocol.

the specific unbinding probability density (SUPD):

$$\mathrm{SUPD}(F_k) \approx 100\,\frac{N_{SB}}{N_{TOT}}\left[\frac{1}{\Delta F}\,\frac{N_k}{N_{SB}}\right] \qquad (1)$$

where N_k is the number of curves in the kth bin whose unbinding force F_{ub} falls within $F_k \pm \Delta F/2$. Its integral *versus* F_{ub} across the data set is estimated as the summation on the histogram bins multiplied by ΔF. The summation index runs from 1 to k_{max}, with k_{max} being the index corresponding to $F_{k_{max}}(F_{ub})$. The $\mathrm{SUP}(F_{max}) = 100 \cdot N_{SB}/N_{TOT}$ is the asymptotic limit of the curves shown in Figure 6f:

$$\mathrm{SUP}(F_{ub}) = \int_0^{F_{ub}} \mathrm{SUPD}(F)\mathrm{d}F \approx 100\left[\sum_{k=1}^{k_{max}} \frac{N_k}{N_{TOT}}\right] \qquad (2)$$

The skewness (standardized third moment) of each data set is found to be significant as its values largely exceed the corresponding Gaussian distribution estimator $(6/N_{SB})^{1/2}$.[55] The three data sets exhibit a mean force value $\langle F^*_{ub}\rangle(\pm\sigma)$ equal to 98 ± 55 , 109 ± 59, and 80 ± 39 pN for PG, HSC_6NH_2, and cross-check samples, respectively. We have inserted these values as parameters in the functional[56,57]

$$\begin{aligned}\mathrm{SUPD}(F_{ub}) &= 100 \cdot \frac{N_{SB}}{N_{TOT}} \cdot \chi^2(F_{ub}) \\ &= 100 \cdot \frac{N_{SB}}{N_{TOT}}\,\frac{1}{2^p\Gamma(p)}\left(\frac{\sqrt{p}\cdot F_{ub}}{\sigma}\right)^{p-1} \\ &\quad \times \exp\left(-\frac{\sqrt{p}\cdot F_{ub}}{\sigma}\right)\end{aligned} \qquad (3)$$

Equation 3 describes a χ^2 distribution normalized to the overall probability to detect a specific unbinding event. Here the parameters are $p = (\langle F^*_{ub}\rangle/\sigma)^2$, and $\Gamma(p)$ is the gamma function. The trends of SUPD, depicted as

TABLE 1

experiment	x_β (Å)	k_{off} (s^{-1})	τ (s)	$\Delta G_{binding}$ (kJ/mol)	μ (% loss)	ΔV_{th} (mV)
IL4 on protein G	3.2 ± 0.2	0.004 ± 0.002	206 ± 103	84 ± 42	16	≈10
IL4 on HSC_6NH_2	2.4 ± 0.1	0.209 ± 0.073	5 ± 2	75 ± 26		

continuous curves overlapping the histograms in Figure 6e, show a conformational adherence within the force range from 20 to 300 pN.[58−62] It is clear that the SUPD curves for both PG and HSC_6NH_2 are alike and can be mapped one onto another by a simple vertical rescaling. On the other hand, they are substantially different from the one of the cross-check sample that has the same shape but whose peak is displaced at lower force values, and they are radically different from the one of the control sample (bare Au) that does not exhibit an apparent skewness. By looking at the SUP, it is clear that anti-IL4/PG/Au induces a frequency of specific binding events 3-fold larger than the sample anti-IL4/HSC_6NH_2/Au (see Figure 6f). These values can be interpreted as the result of the effective coverage of functional Abs on the respective surfaces; that is, PG yields a 30% coverage of available Abs for recognition of IL4, whereas HSC_6NH_2 yields only 10%. The comparison between the two immobilization strategies has been reproduced with another antibody−antigen pair, that is, interleukin-6 (IL6)/anti-IL6 pair, yielding even more marked differences in recognition probability (see Figure S2 in the Supporting Information). Noticeably, the SUP of HSC_6NH_2 is comparable to that of the cross-check sample, although it appears that the latter contributes to events whose force is below 200 pN. This implies that in the cross-check sample it is possible to observe single specific recognition events but not multiple ones, conversely to the other cases. The distribution related to bare gold shows a different trend, and the SUP is much lower than all the other distributions. This means that IL4 poorly interacts with unfunctionalized Au, as expected.

In order to gain insights into the energy landscape of the bound complexes, we carried out experiments at different retraction velocities. According to the Bell−Evans model, the force of a single-energy barrier in the thermally activated regime scales up with the logarithm of the loading rate[28] (see Supporting Information):

$$F_{ub} = \frac{k_B T}{x_\beta} \ln\left(\frac{\nu x_\beta}{k_{off} k_B T}\right) \quad (4)$$

Here, F_{ub} is the most probable unbinding force, ν the loading rate, x_β the position of the energy barrier along the reaction coordinate, k_{off} the dissociation constant at zero force, and k_BT the thermal energy.

The associated values for the Bell−Evans model parameters such as the reaction length x_β and the lifetime of the complex $\tau = 1/k_{off}$ are reported in Table 1. The value of the $k_{off} = 4 \times 10^{-3}\ s^{-1}$, corresponding to $\tau = 206$ s for PG-based functionalization, is in good agreement with the values observed in literature for specific antigen−antibody pairing characterized by single-molecule force spectroscopy.[58,63] For HSC_6NH_2 functionalization, we obtain $k_{off} = 0.209\ s^{-1}$, corresponding to a lifetime $\tau = 5$ s. The almost 2 orders of magnitude ratio of the k_{off} indicates that the antigen fits more steadily with the antibody when the latter is immobilized onto the PG substrate, as compared to the HSC_6NH_2 functionalization.[64,65] This yields the increased binding affinity between IL4/anti-IL4 when PG is used for the antibody immobilization. As far as the potential barrier width between the bound complex and the transition state, x_β, is concerned, the values for both functionalization approaches fall in the range usually found for specific interactions between partners with a rather high conformational stability.[53] We observe that the IL4/anti-IL4 complex formed *via* PG immobilization with a lifetime of the complex of 206 s shows stability higher than that of the one formed onto the SAM-functionalized surface, which will dissociate faster at a complex lifetime of 5 s.

According to the Bell−Evans model, the dissociation of the antibody−antigen complex under an external force is described in the frame of the transition state theory.[17,66] Once k_{off} is calculated, ΔG can be estimated using the following equation, where h is Planck's constant:

$$\Delta G = -k_B T \ln \frac{k_{off} \cdot h}{k_B T} \quad (5)$$

The total free energy of the antibody−antigen complex has been estimated for the two gold functionalization approaches, obtaining values of −91 kJ/mol for the PG-mediated functionalization and −82 kJ/mol for the HSC_6NH_2 functionalization. One should take into account the fact that this free energy includes contribution from the unbinding process of the antibody−antigen complex, as well as from the stretching of the PEG linker. Therefore, the free energy related exclusively to the unbinding process of the IL4/anti-IL4 complex can be calculated from this expression:

$$\Delta G_{ub} = \Delta G_{Ab/Ag} - \Delta G_{PEG} \quad (6)$$

The free energy related to the stretching of a 10 nm long PEG linker has been estimated experimentally to be −7.45 kJ/mol,[67] so the unbinding free energy corresponding to the antibody−antigen pairs is −84 ± 42 kJ/mol for the PG-based functionalization and −75 ± 26 kJ/mol for the HSC_6NH_2 functionalization. These values of the unbinding free energy could be

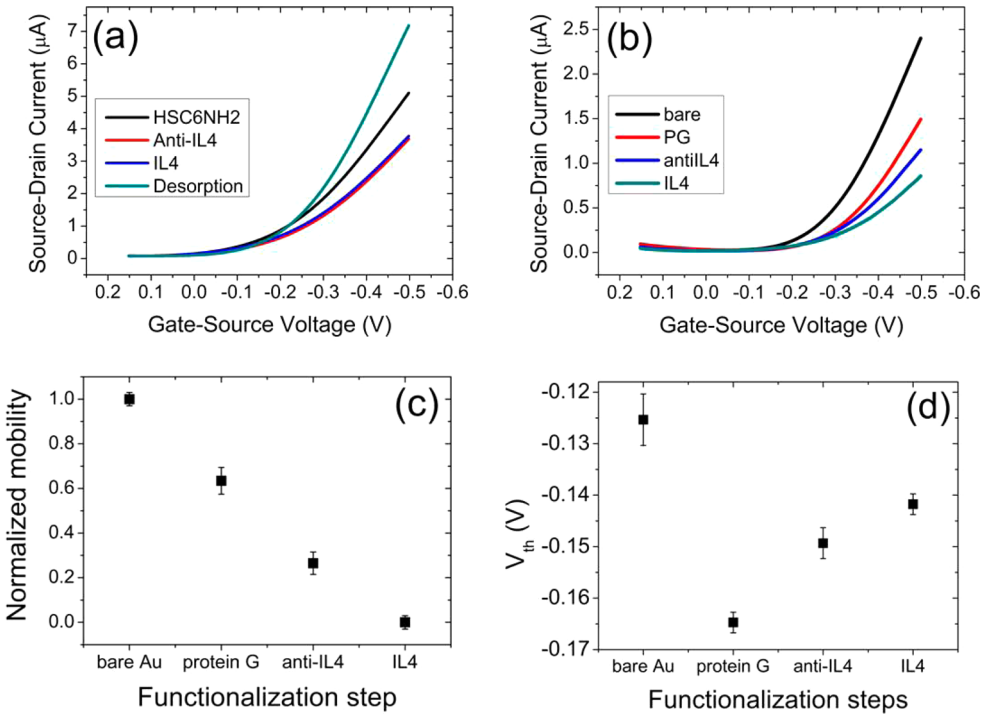

Figure 7. *I*−*V* **transfer characteristics for (a) HSC_6NH_2- and (b) PG-based protocols. Normalized mobility ratio (c) and threshold voltage (d) trends corresponding to the stepwise functionalization.**

related to the breaking of several hydrogen bonds and one or two salt bridges that are responsible for the Ab−Ag recognition.

Detection of IL4 with EGOFET-Based Immunosensors. The pristine device exhibits a field-effect charge mobility $\mu = 3.8 \times 10^{-4}$ cm^2 V^{-1} s^{-1} and a threshold voltage $V_{th} = -125$ mV. The leakage current is always lower than 10 nA along with an almost negligible hysteresis featuring no electrochemical doping of pentacene thin film.

The *I*−*V* characteristics of an immuno-EGOFET with a gate electrode modified with anti-IL4, immobilized by a glutaraldehyde-based protocol, are shown in Figure 7a. We observe that the anti-IL4 (red curve) induces an electrical change in the *I*−*V* curve with respect to that recorded before anti-IL4 immobilization (black curve). The Au gate electrode was then incubated in a reference solution of IL4 at a concentration of 5 nM. This additional exposure does not give rise to further electrical change (blue curve). According to the protocol of Porter *et al.*,[68,69] the biological layer has been electrochemically detached (see Figure S3 in Supporting Information) *via* the cleavage of the chemical bond between Au and sulfur of the 6-aminohexanethiol. The subsequent increase of the EGOFET performance proves that no deterioration is taking place at the experimental time scale. The same validation process has been applied to the PG-based protocol (see Figure 3b). At variance with the previously described case, a significant change in the electrical response is now observed after incubation of the gate electrode in the IL4 solution.

We then focused our attention only on the PG-mediated functionalization and monitored step-by-step changes in the electrical performances of the device by recording shifts of μ and V_{th} (see Figure 7c,d). Throughout the functionalization procedure, mobility shows a gradual decrease down to 60% of the initial value. This is ascribed to a decrease of the capacitive coupling between the gate electrode and the organic semiconductor thin film due to addition of biological layers on the gate surface (see Figure 7c). Regarding the threshold voltage, a rather complex behavior has been observed. On one hand, the adsorption of protein G gives rise to a negative shift of threshold voltage, while on the other hand, both anti-IL4 grafting and subsequently IL4 recognition yield an opposite shift. This means that the protein G reduces the charge carrier density in the conductive channel with respect to bare Au electrode. Due to the fact that the isoelectric point (pI) of protein G is acidic (around 5), this means that protein G is negatively charged at pH 7.2 and strongly coupled to the charge carriers in the channel to act as a trap and not as a dopant. In the case of IL4, whose pI is 8.2, there is a partial release of these "trapped" carriers, manifesting itself with a shift toward less negative threshold voltage. This can be due either to formation of a surface dipole upon specific binding of IL4 to its anti-IL4, thus increasing the capacitance of the interface and the consequent capacitive coupling, or to a partial compensation of the negative charge density of protein G.

Our electrical measurements show that PG-functionalized EGOFETs are capable of sensing IL4

down to 5 nM concentrations, while the HSC_6NH_2-functionalized device does not give a measurable response. The PG-functionalized device shows a mobility loss of 16% and a positive shift in the threshold voltage of approximately 10 mV after exposure to an IL4 solution (see Table 1). The absence of significant changes in the electrical properties of EGOFETs with gate electrodes modified with the HSC_6NH_2-based functionalization is consistent with the much lower probability of recognition events for randomly oriented anti-IL4.

CONCLUSIONS

The use of two completely different techniques in terms of spatial and temporal scales, such as electrical measurements by using organic transistors and single-molecule force spectroscopy, allowed us to draw a direct correlation between them in the study of specific interactions of the antibody−antigen pair. For this purpose, two strategies of surface functionalization have been assessed: one based on the use of amino-terminated self-assembled monolayers and another one by means of His-tagged protein G. Single force spectroscopy measurements allowed us to detect a larger probability (30%) of unbinding events for PG-based strategy with respect to 6-aminohexanethiol-based one (10%). Furthermore, by using single-force spectroscopy, we could obtain an average lifetime of the antibody−antigen complex for the two different strategies, and we found that the anti-IL4/PG/Au interface shows a lifetime (τ = 206 ± 103 s) significantly higher than that of the anti-IL4/HSC_6NH_2/Au ($\tau = 5 \pm 2$ s). This experimental evidence clearly proves how PG yields a more ordered Ab layer, hence a more crowded surface of active Abs toward IL4. The direct implementation of these Au electrodes in the EGOFET architecture confirms different sensitivities as a function of the functionalization strategies. As a result, EGOFET successfully sensed IL4 down to 5 nM concentration when the gate electrode was functionalized by PG, whereas EGOFETs functionalized by 6-aminohexanethiol failed. Finally, our comparative study meets the challenging task to correlate a mechanical nanoscale metrology by using SFS to probe individual or a few Ab−Ag pairings with the electrical EGOFET response that involves a wide number of recognition events.

EXPERIMENTAL METHODS

Device Fabrication. Our devices were prepared onto gold-coated glass slides purchased from Phasis (Switzerland). These substrates were made of quartz glass (1 mm thick) and a gold layer of 50 nm plus a few nanometers of titanium as an adhesive layer. Each test pattern contained four transistors, whose channel length was 15 μm and channel width equaled 27 000 μm. The fabrication was carried out by laser ablation with a short-pulsed Nd:YAG infrared (IR) laser supplied by a laser scan marker (Scriba Nanotecnologie S.r.l., Bologna, Italy). The IR laser pulse frequency and intensity were optimized in order to find the best compromise between removal of the Au layer and roughening of the underlying quartz. Typical operation was performed at a laser power of 8300 W, a pulse of 10 ns, and a frequency of 15 500 Hz. The laser focus was moved over the surface at a scan rate of 2000 μm/s. Details are described elsewhere.[70] The pentacene deposition was performed by thermal sublimation in ultrahigh vacuum with a base pressure of 5×10^{-8} mbar at a rate of 7.5 Å min^{-1} on the substrate held at room temperature. The pentacene was 15 nm thick (~10 monolayers, ML) as previously published.[71]

Gate Functionalization. 6-Aminohexanethiol (HSC_6NH_2) and glutaraldehyde were purchased from Sigma-Aldrich and used without further purification. Recombinant PG, monoclonal anti-murine IL4 (anti-IL4), and recombinant murine IL4 were purchased from Vinci-Biochem S.r.l. (Firenze, Italy). These biological species were produced by Biovision (San Francisco, USA). His-tagged recombinant protein G lacked the albumin and cell membrane binding domains.

The gate electrode was a polycrystalline Au wire (diameter equal to 1 mm). First, this electrode underwent a standard cleaning procedure:[71] (i) immersion in a concentrated H_2SO_4 at 100 °C for 1 h; (ii) 20 cycles of electro-polishing by sweeping the potential from 0 to 1.5 V in H_2SO_4 (1 M). The glutaraldehyde-based functionalization occurred by immersing the gate electrode in a 6-aminohexanethiol solution (1 mM) overnight. Further activation was achieved by using glutaraldehyde solution (2.5% v/v) for 1 h at 5 °C, and then the functionalized electrode was immersed in an antibody solution (0.25 mg/mL anti-IL4) for 1 h at 5 °C. The last step consisted of immersing the Ab-coated electrodes in buffer solution (100 mM PBS, pH 7.4) and IL4 (5 nM). The other functionalization exploited a buffer solution (100 mM of PBS, pH 7.4) of protein G (5 mg/mL). Ab and Ag solutions were the same as the previous protocol.

Electrical Measurements. All of the electrochemical, morphological, and mechanical investigations described so far proved the possibility of successfully immobilizing anti-IL4 antibodies on functionalized gold surfaces. SFS experiments have also suggested that the use of PG-based immobilization protocol significantly enhances the probability of recognition events between the surface coated with anti-IL4 and IL4. We then applied these immobilization strategies to the functionalization of the gate Au electrode of EGOFETs to obtain an immunosensor. Our aim is to establish the minimum detection level of IL4 in test solutions and assess whether these concentration ranges are comparable with biologically relevant ones. We compared the electrical responses of EGOFETs with gate electrodes functionalized with the different protocols to assess whether controlling the orientation of the Abs on the surface would enhance the sensing capability of the immunosensors.

All electrical measurements were performed with home-built EGOFETs. As mentioned, the electronic transducer was fabricated by means of laser ablation.[70] Particular attention has been paid to maximize the *W*/*L* ratio, which is the geometrical parameter scaling the drain−source current (I_{DS}). This home-built EGOFET has been operated in a buffer solution (100 mM of PBS at pH 7), mimicking the physiological conditions. The buffer solution has been confined on top of the electronic transducer by means of a PDMS pool, as shown in the cross section of Figure 2.

Source, drain, and gate electrodes were connected to a Keithley 2612 source meter. The electrical response was acquired by means of a probe station. All electrical measurements were carried out in ambient atmosphere. The *I*−*V* transfer characteristics were performed by sweeping the gate−source voltage (V_{GS}) from +0.2 to −0.5 V while leaving the drain−source voltage constant at −0.5 V (saturation regime) for the reference device. The *I*−*V* output characteristics were carried out by sweeping drain−source voltage (V_{DS}) from 0 to −0.5 V

and V_{GS} from 0 to −0.5 V with a step of 0.1 V. The V_{GS} scan rates were 20 and 80 mV/s for transfer and output characteristics, respectively.

Electrochemical measurements were performed by a usual three-electrode cell connected to a potentiostat/galvanostat μ-Autolab type III (Metrohm Italiana S.r.l., Varese, Italy), using a polycrystalline Au wire as working electrode, functionalized with the above-mentioned protocols; a Pt sheet and Ag/AgCl were used as counter and reference electrodes, respectively.

The impedance response was fitted by Randles circuit, which is an equivalent circuit composed by an electrolyte solution resistance, R_S, a charge transfer resistance, R_{CT}, a Debye−Helmhotz capacitance, C_{DL}, and a Warburg element, W.

Single-Molecule Force Spectroscopy. In these experiments, the force dependence on the probe surface distance was recorded (*viz*. force curve), as shown in Figure 1. A force curve contained regions that show a smooth variation with the distance. Those regions were interrupted by the presence of sharp changes in the force, which are associated with molecular recognition interactions, interpreted as the rupture of one or several bonds. The forces measured by force spectroscopy are dynamic in nature, as they depend on the loading rate[27,28] and electrostatic interactions.[19] To a certain extent, the electrostatic interactions are controlled by the immobilization protocols applied to a biospecies of interests on a certain substrate.

Tip Functionalization. Phosphate buffer saline powder, which yields 0.01 M phosphate buffered saline (NaCl 0.138 M; KCl 0.0027 M) when dissolved in 1 L of water, hydrogen peroxide 30%, sulfuric acid, 3-aminopropyltriethoxysilane (APTES), glutaraldehyde 8%, 6-aminohexanethiol, and ethanol were purchased from Sigma-Aldrich. The 24-unit ethylene glycol functionalized with succinimidyl and maleimido ends (NHS-PEG_{24}-Mal) and the sulfhydryl addition kit containing SATA (*N*-succinimidyl-*S*-acetylthioacetate)hydroxylamine·HCl, conjugation buffer stock (10×), dimethylformamide (DMF), and dextran desalting column were purchased from Thermo Scientific. Recombinant protein G, monoclonal antimurine IL4, and recombinant murine IL4 were produced by Biovision (San Francisco, USA).

AFM silicon nitride tips were first cleaned thoroughly by immersion in a piranha solution (3:1 concentrated sulfuric acid to 30% hydrogen peroxide solution) for 30 min. They were then rinsed with nanopure water and dipped into a solution of APTES/water/ethanol (ratio 5:5:95 v/v) for 30 min. Finally, the amino-functionalized tips were rinsed with nanopure water and ethanol and dried in nitrogen.

Next, the heterobifunctional NHS-PEG_{24}-Mal linker was reacted with the antigen bearing a sulfhydryl group. Prior to that, a free sulfhydryl functionality was added to the antigen using the SATA reagent. A 17.3 mM SATA solution in DMF was added in 10-fold molar excess to 1 mL of protein. The reaction was incubated for 30 min at room temperature. Then, 5 mg of hydroxylamine·HCl was mixed with 100 μL of conjugation buffer stock (10×). To deprotect the latent sulfhydryl, 100 μL of hydroxylamine solution was added to the SATA-modified protein, and the mixture was incubated for 2 h at room temperature. The deprotected sulfhydryl protein was then added to the equilibrated desalting column to remove nonreacted reagents. The maleimide conjugation buffer was added to the desalting column, and 1 mL fractions were collected; the absorbance of each fraction was measured at 280 nm to locate the protein. Fractions containing most of the protein were then reacted with the NHS-PEG_{24}-Mal linker. A 10-fold molar excess of the PEG linker was incubated with the sulfhydryl-modified antigen at 4 °C for 12 h. Finally, the amino-functionalized AFM tips were immersed in the PEG−antigen solution for 2 h at room temperature. The tips were rinsed with PBS 0.1 M and stored in a Petri dish at 4 °C until further usage.

Substrate Functionalization. The substrates used were mica sheets covered with a 3 nm adhesive Cr layer and a 50 nm thick gold layer. The antibody immobilization onto the gold substrate has been performed by following the same protocols used for the gate functionalization.

Topography Measurements. Tapping mode AFM was employed to record topographical images of the samples at different functionalization steps in both air and PBS.[72] Rectangular PPP-NCH (Nanoworld AG, Switzerland) cantilevers with a nominal force constant of k = 40 N m^{-1} and a resonant frequency of 291 kHz have been used for air measurements. For the experiments in a liquid environment, rectangular OMCL-RC800PSA (Olympus, Japan) with a nominal force constant of 0.4 N/m and a resonant frequency of 33 kHz were employed. The topography measurements were performed in amplitude modulation AFM by mechanically driving the cantilever.[73]

Single-Molecule Force Spectroscopy Measurements. Single-molecule force spectroscopy experiments were performed with a Multimode atomic force microscope fitted with a Nanoscope V controller (Bruker, Santa Barbara). The microscope was equipped with a liquid cell where approximately 60 μL of PBS 0.01 M, pH 7.4, was introduced in order to carry out the measurements. Triangular OTR-4 silicon nitride tips (Bruker, Santa Barbara) with a spring constant of 0.015−0.08 N/m and resonant frequency of 1.8 kHz and 8 kHz were used. The force constant and quality factor were determined by using the thermal noise method.[74] At the end of each experiment, the optical lever sensitivity was calibrated by acquiring deflection *versus* distance curves on a hard surface (mica). Typically, 100 deflection *versus* distance curves were acquired, and the sensitivity of the photodiode was calculated as the mean value. The force was calculated using Hooke's law: $F = -kd$ (d is cantilever deflection, k is cantilever force constant). The applied force was maintained below 600 pN.

The force curves were acquired in static mode by approaching and retracting the tip toward the sample by 200 nm at different velocities (0.5, 1, 2, and 5 Hz). Each time, the tip was kept in contact with the sample for 0.5 s in order to favor the recognition process.

Several rounds of control experiments have been performed to check the specificity of the unbinding events. On one hand, force curves of a bare AFM tip interacting with the substrate at each functionalization step for both protocols were recorded. Afterward, antigen-tethering AFM tips were tested against Au, anti-IL4/HSC_6NH_2/Au, and anti-IL4/PG/Au. On the other hand, cross-reactivity experiments have been performed by bringing IL4 antibodies on the substrate in contact with the IL6 antigen on the tip.

Dynamic Force Spectroscopy Data Analysis. A total of 16 297 force distance curves were analyzed by using customized software in an automated way. The curves were averaged, and the contact point was set according to a deflection threshold. Event recognition was based on the values of the second and third derivatives of the deflection; the event was labeled as a recognition event whenever the derivatives were found to be above a threshold with respect to the noise level. An algorithm was created to discriminate specific recognition events from surface adhesion events. The algorithm was based on the calculation of the deviation between the deflection curve and the straight line that goes from the peak minimum to the contact with the surface (see Supporting Information Figure S4). Tables containing information on specific events for all the experiments were processed, and 1D and 2D histograms were extracted.

The dynamics of the IL4 antibody−antigen binding were explored by determining the unbinding force as a function of the unbinding rate. The loading rate was the product between the retract velocity and the spring constant. To account for the contribution of the PEG linker spring constant to the overall spring constant of the system, the loading rate was extracted from the slope of the force curve before unbinding occurred. The plots in Figure S5 display the linear increase of the most probable unbinding force with the logarithm of the loading rate for the two antibody immobilization protocols. This characteristic behavior for a thermally activated dissociation process under an applied load has been previously observed for other antibody−antigen complexes.

To determine the kinetic parameters of the molecular recognition process, the length of the energy barrier, x_β, was determined from the slope of the linear fit of the unbinding forces *versus* loading rate logarithm plot (see eq 1). Next, the kinetic off-rate constant of dissociation at zero force was calculated by extrapolation to zero forces. Antibody−antigen

complexes have limited lifetimes, which are shortened by thermal activation under an applied force. The characteristic time needed for the spontaneous dissociation, τ, was given by the inverse of the kinetic off-rate constant and can be correlated with the specificity of the recognition process as well as the stability of the complex.

Conflict of Interest: The authors declare no competing financial interest.

Acknowledgment. We thank Prof. Francesco Zerbetto, Alma Mater-Università di Bologna, for useful discussions. This work was supported by the EU-project I-ONE-FP7 "Implantable Organic Nano-Materials" NMP4-SL-2012, Grant Agreement No. 280772. R.F.O. acknowledges financial support from FAPESP (Brazil) through project Proc. 2013/03857-0. A.C.D. acknowledges financial support from MINECO (Spain) through project CSD2010-00024.

Supporting Information Available: Overlay of double-layer capacitance (C_{DL}) and charge transfer resistance (R_{CT}) corresponding to PG adsorption/desorption; table of C_{DL} and R_{CT} values for the two functionalization protocol; histograms and bar plot of the probability corresponding to IL6 immunorecognition; cyclic voltammogram of reductive electrodesorption; scheme of the algorithm mechanism; unbinding force *vs* loading rate plot. This material is available free of charge *via* the Internet at http://pubs.acs.org.

REFERENCES AND NOTES

1. Mariuzza, R. A.; Immunologie, D.; Pasteur, I.; Cedex, P. The Structural Basis of Antigen–Antibody Recognition. *Annu. Rev. Biophys. Biophys. Chem.* **1987**, *16*, 139–159.
2. Van Weemen, B. K.; Schuurs, A. H. Immunoassay Using Antigen–Enzyme Conjugates. *FEBS Lett.* **1971**, *15*, 232–236.
3. Marquette, C. A.; Blum, L. J. State of the Art and Recent Advances in Immunoanalytical Systems. *Biosens. Bioelectron.* **2006**, *21*, 1424–1433.
4. Hock, B. Antibodies for Immunosensors a Review. *Anal. Chim. Acta* **1997**, *347*, 177–186.
5. Kurosawa, S.; Park, J.-W.; Aizawa, H.; Wakida, S.-I.; Tao, H.; Ishihara, K. Quartz Crystal Microbalance Immunosensors for Environmental Monitoring. *Biosens. Bioelectron.* **2006**, *22*, 473–481.
6. Butt, .; Skla, P.; Raiteri, R.; Grattarola, M. Micromechanical Cantilever-Based Biosensors. *Sens. Actuators* **2001**, *79*, 115–126.
7. Guilbault, G. G.; Amia, F. Recent Developments in Piezoelectric Immunosensors* A Review. *Analyst* **1994**, *11*, 2279–2282.
8. Abdulhalim, I.; Zourob, M.; Lakhtakia, A. Surface Plasmon Resonance for Biosensing: A Mini-Review. *Electromagnetics* **2008**, *28*, 214–242.
9. Lee, C.-S.; Kim, S. K.; Kim, M. Ion-Sensitive Field-Effect Transistor for Biological Sensing. *Sensors* **2009**, *9*, 7111–7131.
10. Liang, K.; Mu, W.; Huang, M.; Yu, Z.; Lai, Q. Interdigitated Conductometric Immunosensor for Determination of Interleukin-6 in Humans Based on Dendrimer G4 and Colloidal Gold Modified Composite Film. *Electroanalysis* **2006**, *18*, 1505–1510.
11. Yang, L.; Li, Y.; Erf, G. F. Interdigitated Array Microelectrode-Based Electrochemical Impedance Immunosensor for Detection of *Escherichia coli* O157: H7. *Anal. Chem.* **2004**, *76*, 1107–1113.
12. Hays, H. C. W.; Millner, P. A.; Prodromidis, M. I. Development of Capacitance Based Immunosensors on Mixed Self-Assembled Monolayers. *Sens. Actuators, B* **2006**, *114*, 1064–1070.
13. Wan, Y.; Su, Y.; Zhu, X.; Liu, G.; Fan, C. Development of Electrochemical Immunosensors towards Point of Care Diagnostics. *Biosens. Bioelectron.* **2013**, *47*, 1–11.
14. Casal, P.; Wen, X.; Gupta, S.; Nicholson, T.; Wang, Y.; Theiss, A.; Bhushan, B.; Brillson, L.; Lu, W.; Lee, S. C. ImmunoFET Feasibility in Physiological Salt Environments. *Philos. Trans. R. Soc., A* **2012**, *370*, 2474–2488.
15. Palazzo, G.; De Tullio, D.; Magliulo, M.; Mallardi, A.; Intranuovo, F.; Mulla, M. Y.; Favia, P.; Vikholm-Lundin, I.; Torsi, L. Detection Beyond Debye's Length with an Electrolyte-Gated Organic Field-Effect Transistor. *Adv. Mater.* **2014**, *27*, 911–916.
16. Sheehan, A. D.; Quinn, J.; Daly, S.; Dillon, P.; O'Kennedy, R. The Development of Novel Miniaturized Immuno-Sensing Devices: A Review of a Small Technology with a Large Future. *Anal. Lett.* **2003**, *36*, 511–537.
17. Evans, E.; Ritchie, K. Dynamic Strength of Molecular Adhesion Bonds. *Biophys. J.* **1997**, *72*, 1541–1555.
18. Merkel, R.; Nassoy, P.; Leung, A.; Ritchie, K.; Evans, E. Energy Landscapes of Receptor–Ligand Bonds Explored with Dynamic Force Spectroscopy. *Nature* **1999**, *397*, 50–53.
19. Medalsy, I. D.; Müller, D. J. Nanomechanical Properties of Proteins and Membranes Depend on Loading Rate and Electrostatic Interactions. *ACS Nano* **2013**, *7*, 2642–2650.
20. Florin, E. L.; Moy, V. T.; Gaub, H. E. Adhesion Forces between Individual Ligand-Receptor Pairs. *Science* **1994**, *264*, 415–417.
21. Moy, V. T.; Florin, E. L.; Gaub, H. E. Intermolecular Forces and Energies between Ligands and Receptors. *Science* **1994**, *266*, 257–259.
22. Hinterdorfer, P.; Baumgartner, W.; Gruber, H. J.; Schilcher, K.; Schindler, H. Detection and Localization of Individual Antibody–Antigen Recognition Events by Atomic Force Microscopy. *Proc. Natl. Acad. Sci. U.S.A.* **1996**, *93*, 3477–3481.
23. Brogan, K. L.; Schoenfisch, M. H. Influence of Antibody Immobilization Strategy on Molecular Recognition Force Microscopy Measurements. *Langmuir* **2005**, *21*, 3054–3060.
24. Carrion-Vazquez, M.; Oberhauser, A. F.; Fowler, S. B.; Marszalek, P. E.; Broedel, S. E.; Clarke, J.; Fernandez, J. M. Mechanical and Chemical Unfolding of a Single Protein: A Comparison. *Proc. Natl. Acad. Sci. U.S.A.* **1999**, *96*, 3694–3699.
25. Rief, M.; Gautel, M.; Oesterhelt, F.; Fernandez, J. M.; Gaub, H. E. Reversible Unfolding of Individual Titin Immunoglobulin Domains by AFM. *Science* **1997**, *276*, 1109–1112.
26. Tromas, C.; Rojo, J.; de la Fuente, J. M.; Barrientos, A. G.; García, R.; Penadés, S. Adhesion Forces between LewisX Determinant Antigens As Measured by Atomic Force Microscopy. *Angew. Chem., Int. Ed.* **2001**, *40*, 3052–3055.
27. Müller, D. J.; Dufrêne, Y. F. Force Nanoscopy of Living Cells. *Curr. Biol.* **2011**, *21*, R212–R216.
28. Campana, A.; Cramer, T.; Simon, D. T.; Berggren, M.; Biscarini, F. Electrocardiographic Recording with Conformable Organic Electrochemical Transistor Fabricated on Resorbable Bioscaffold. *Adv. Mater.* **2014**, *26*, 3874–3878.
29. Cramer, T.; Chelli, B.; Murgia, M.; Barbalinardo, M.; Bystrenova, E.; de Leeuw, D. M.; Biscarini, F. Organic Ultra-thin Film Transistors with a Liquid Gate for Extracellular Stimulation and Recording of Electric Activity of Stem Cell-Derived Neuronal Networks. *Phys. Chem. Chem. Phys.* **2013**, *15*, 3897–3905.
30. Khodagholy, D.; Doublet, T.; Quilichini, P.; Gurfinkel, M.; Leleux, P.; Ghestem, A.; Ismailova, E.; Hervé, T.; Sanaur, S.; Bernard, C.; et al. *In Vivo* Recordings of Brain Activity Using Organic Transistors. *Nat. Commun.* **2013**, *4*, 1–7.
31. Cramer, T.; Kyndiah, A.; Murgia, M.; Leonardi, F.; Casalini, S.; Biscarini, F. Double Layer Capacitance Measured by Organic Field Effect Transistor Operated in Water. *Appl. Phys. Lett.* **2012**, *100*, 143302.
32. Cramer, T.; Campana, A.; Leonardi, F.; Casalini, S.; Kyndiah, A.; Murgia, M.; Biscarini, F. Water-Gated Organic Field Effect Transistors: Opportunities for Biochemical Sensing and Extracellular Signal Transduction. *J. Mater. Chem. B* **2013**, *1*, 3728–3741.
33. Casalini, S.; Leonardi, F.; Cramer, T.; Biscarini, F. Organic Field-Effect Transistor for Label-Free Dopamine Sensing. *Org. Electron.* **2013**, *14*, 156–163.
34. Kergoat, L.; Piro, B.; Berggren, M.; Pham, M.-C.; Yassar, A.; Horowitz, G. DNA Detection with a Water-Gated Organic Field-Effect Transistor. *Org. Electron.* **2012**, *13*, 1–6.
35. Buth, F.; Kumar, D.; Stutzmann, M.; Garrido, J. A. Electrolyte-Gated Organic Field-Effect Transistors for Sensing Applications. *Appl. Phys. Lett.* **2011**, *98*, 153302.

36. Buth, F.; Donner, A.; Sachsenhauser, M.; Stutzmann, M.; Garrido, J. A. Biofunctional Electrolyte-Gated Organic Field-Effect Transistors. *Adv. Mater.* **2012**, *24*, 4511–4517.
37. Magliulo, M.; Mallardi, A.; Mulla, M. Y.; Cotrone, S.; Pistillo, B. R.; Favia, P.; Vikholm-Lundin, I.; Palazzo, G.; Torsi, L. Electrolyte-Gated Organic Field-Effect Transistor Sensors Based on Supported Biotinylated Phospholipid Bilayer. *Adv. Mater.* **2012**, *25*, 2090–2094.
38. Ledeboer, A.; Brevé, J. J. P.; Poole, S.; Tilders, F. J. H.; Dam, A. V. A. N. Interleukin-10, Interleukin-4 and Transforming Growth Factor-Beta Differentially Regulate Lipopolysaccharide-Induced Production of Pro-inflammatory Cytokines and Nitric Oxide in Co-cultures of Rat Astroglial and Microglial Cells. *Glia* **2000**, *30*, 134–142.
39. Wirjatijasa, F.; Dehghani, F.; Blaheta, R. A.; Korf, H.-W.; Hailer, N. P. Interleukin-4, Interleukin-10, and Interleukin-1-Receptor Antagonist but Not Transforming Growth Factor-Beta Induce Ramification and Reduce Adhesion Molecule Expression of Rat Microglial Cells. *J. Neurosci. Res.* **2002**, *68*, 579–587.
40. Yang, M.-S.; Park, E. J.; Sohn, S.; Kwon, H. J.; Shin, W.-H.; Pyo, H. K.; Jin, B.; Choi, K. S.; Jou, I.; Joe, E.-H. Interleukin-13 and -4 Induce Death of Activated Microglia. *Glia* **2002**, *38*, 273–280.
41. Lee, S. I.; Jeong, S. R.; Kang, Y. M.; Han, D. H.; Jin, B. K.; Namgung, U.; Kim, B. G. Endogenous Expression of Interleukin-4 Regulates Macrophage Activation and Confines Cavity Formation after Traumatic Spinal Cord Injury. *J. Neurosci. Res.* **2010**, *88*, 2409–2419.
42. Betancor, L.; López-Gallego, F.; Hidalgo, A.; Alonso-Morales, N.; Mateo, G. D.-O. C.; Fernández-Lafuente, R.; Guisán, J. M. Different Mechanisms of Protein Immobilization on Glutaraldehyde Activated Supports: Effect of Support Activation and Immobilization Conditions. *Enzyme Microb. Technol.* **2006**, *39*, 877–882.
43. Walt, D. R.; Agayn, V. I. The Chemistry of Enzyme and Protein Immobilization with Glutaraldehyde. *Trends Anal. Chem.* **1994**, *13*, 425–430.
44. Yang, Z.; Zhao, Y.-P. Adsorption of His-Tagged Peptide to Ni, Cu and Au (100) Surfaces: Molecular Dynamics Simulation. *Eng. Anal. Boundary Elem.* **2007**, *31*, 402–409.
45. Soong, R. K.; Stelick, S. J.; Bachand, G. D.; Montemagno, C. D. Evaluating Adhesion Strength of Biological Molecules to Nanofabricated Substrates. *Int. Conf. Model. Simul. Microsyst.* **1999**, 95–98.
46. Bachand, G. D.; Montemagno, C. D. Constructing Organic/Inorganic NEMS Devices Powered by Biomolecular Motors. *Biomed. Microdev.* **2000**, *2:3*, 179–184.
47. Baio, J. E.; Cheng, F.; Ratner, D. M.; Stayton, P. S.; Castner, D. G. Probing Orientation of Immobilized Humanized Anti-lysozyme Variable Fragment by Time-of-Flight Secondary-Ion Mass Spectrometry. *J. Biomed. Mater. Res., Part A* **2011**, *97*, 1–7.
48. Trilling, A. K.; Beekwilder, J.; Zuilhof, H. Antibody Orientation on Biosensor Surfaces: A Minireview. *Analyst* **2013**, *138*, 1619–1627.
49. Bae, Y. M.; Oh, B.-K.; Lee, W.; Lee, W. H.; Choi, J.-W. Study on Orientation of Immunoglobulin G on Protein G Layer. *Biosens. Bioelectron.* **2005**, *21*, 103–110.
50. Song, H. Y.; Zhou, X.; Hobley, J.; Su, X. Comparative Study of Random and Oriented Antibody Immobilization As Measured by Dual Polarization Interferometry and Surface Plasmon Resonance Spectroscopy. *Langmuir* **2012**, *28*, 997–1004.
51. Mark, L. W.; Smith, D. A. Complex Chemical Force Titration Behavior of Amine-Terminated Self-Assembled Monolayers. *Langmuir* **2001**, *17*, 1126–1131.
52. San Paulo, A.; García, R. Attractive and Repulsive Tip–Sample Interaction Regimes in Tapping-Mode Atomic Force Microscopy. *Phys. Rev. B* **1999**, *60*, 4961–4967.
53. Zhao, X.; Yaseen, M.; Pan, F.; Lu, J. R.; Street, M.; Sheffield, S. *Protein and Interfaces III. State of the Art*, ACS Symposium Series; American Chemical Society: Washington, DC, 2012; pp 543–574.
54. Ido, S.; Kimiya, H.; Kobayashi, K.; Kominami, H.; Matsushige, K.; Yamada, H. Immunoactive Two-Dimensional Self-Assembly of Monoclonal Antibodies in Aqueous Solution Revealed by Atomic Force Microscopy. *Nat. Mater.* **2014**, *13*, 264–270.
55. Press, W. H.; Teukolsky, S. A.; Vetterling, W. T.; Flannery, B. P. *Numerical Recipes, The Art of Scientific Computing*, 3rd ed.; Cambridge University Press: Cambridge, UK, 2007.
56. Abramowitz, M.; Stegun, I. A. *Handbook of Mathematical Functions with Formulas, Graphs, and Mathematical Tables*; Dover Publications: Mineola, NY, 1972.
57. Biscarini, F.; Zamboni, R.; Samorì, P.; Ostoja, P.; Taliani, C. Growth of Conjugated Oligomer Thin Films Studied by Atomic-Force Microscopy. *Phys. Rev. B* **1995**, *52*, 14868–14877.
58. Schwesinger, F.; Ros, R.; Strunz, T.; Anselmetti, D.; Güntherodt, H.-J.; Honegger, A.; Jermutus, L.; Tiefenauer, L.; Plückthun, A. Unbinding Forces of Single Antibody–Antigen Complexes Correlate with Their Thermal Dissociation Rates. *Proc. Natl. Acad. Sci. U.S.A.* **2000**, *97*, 9972–9977.
59. Brogan, K. L.; Shin, J. H.; Schoenfisch, M. H. Influence of Surfactants and Antibody Immobilization Strategy on Reducing Nonspecific Protein Interactions for Molecular Recognition Force Microscopy. *Langmuir* **2004**, *20*, 9729–9735.
60. Berquand, A.; Xia, N.; Castner, D. G.; Clare, B. H.; Abbott, N. L.; Dupres, V.; Adriaensen, Y.; Dufrene, Y. F. Antigen Binding Forces of Single Antilysozyme Fv Fragments Explored by Atomic Force Microscopy. *Langmuir* **2005**, *21*, 5517–5523.
61. Kienberger, F.; Kada, G.; Mueller, H.; Hinterdorfer, P. Single Molecule Studies of Antibody–Antigen Interaction Strength *versus* Intra-molecular Antigen Stability. *J. Mol. Biol.* **2005**, *347*, 597–606.
62. Van Es, M. H.; Tang, J.; Preiner, J.; Hinterdorfer, P.; Oosterkamp, T. H. Single Molecule Binding Dynamics Measured with Atomic Force Microscopy. *Ultramicroscopy* **2014**, *140*, 32–36.
63. Bizzarri, A. R.; Cannistraro, S. The Application of Atomic Force Spectroscopy to the Study of Biological Complexes Undergoing a Biorecognition Process. *Chem. Soc. Rev.* **2010**, *39*, 734–749.
64. Bonanni, B.; Bizzarri, A. R.; Cannistraro, S. Optimized Biorecognition of Cytochrome *c* 551 and Azurin Immobilized on Thiol-Terminated Monolayers Assembled on Au(111) Substrates. *J. Phys. Chem. B* **2006**, *110*, 14574–14580.
65. Bonanni, B.; Kamruzzahan, A. S. M.; Bizzarri, A. R.; Rankl, C.; Gruber, H. J.; Hinterdorfer, P. Single Molecule Recognition between Cytochrome *c* 551 and Gold-Immobilized Azurin by Force Spectroscopy. *Biophys. J.* **2005**, *89*, 2783–2791.
66. Eyring, H. The Activated Complex in Chemical Reactions. *J. Chem. Phys.* **1935**, *3*, 107–115.
67. Oesterhelt, F.; Rief, M.; Gaub, H. E. Single Molecule Force Spectroscopy by AFM Indicates Helical Structure of Poly-(ethylene-glycol) in Water. *New J. Phys.* **1999**, *1*, 6.1–6.11.
68. Walczak, M.; Popenoe, D. D.; Deinhammer, R. S.; Lamp, B. D.; Chung, C.; Porter, M. D. Reductive Desorption of Alkanethiolate Monolayers at Gold: A Measure of Surface Coverage. *Langmuir* **1991**, *7*, 2687–2693.
69. Widrig, A.; Porter, M. D. The Electrochemical Desorption of *N*-Alkanethiol from Polycrystalline Au and Ag Electrodes Monolayers. *J. Electroanal. Chem.* **1991**, *310*, 335–359.
70. Campana, A.; Cramer, T.; Greco, P.; Foschi, G.; Murgia, M.; Biscarini, F. Facile Maskless Fabrication of Organic Field Effect Transistors on Biodegradable Substrates. *Appl. Phys. Lett.* **2013**, *103*, 073302.
71. Casalini, S.; Shehu, A.; Destri, S.; Porzio, W.; Pasini, M. C.; Vignali, F.; Borgatti, F.; Albonetti, C.; Leonardi, F.; Biscarini, F. Organic Field-Effect Transistors as New Paradigm for Large-Area Molecular Junctions. *Org. Electron.* **2012**, *13*, 789–795.
72. Garcia, R.; San Paulo, A. Attractive and Repulsive Tip–Sample Interaction Regimes in Tapping-Mode Atomic Force Microscopy. *Phys. Rev. B* **1999**, *60*, 4961–4967.
73. Herruzo, E. T.; Garcia, R. Frequency Response of an Atomic Force Microscope in Liquids and Air: Magnetic *versus* Acoustic Excitation. *Appl. Phys. Lett.* **2007**, *91*, 143113.
74. Butt, H.-J.; Jaschke, M. Calculation of Thermal Noise in Atomic Force Microscopy. *Nanotechnology* **1995**, *6*, 1–7.